The global climatology of the intensity of the ionospheric sporadic E layer

Bingkun Yu[1,2], Xianghui Xue[1,2,3], Xin'an Yue[4], Chengyun Yang[1,2], Chao Yu[1,2], Xiankang Dou[1,2], Baiqi Ning[4], and Lianhuan Hu[4]

[1]CAS Key Laboratory of Geospace Environment, Department of Geophysics and Planetary Sciences, University of Science and Technology of China, Hefei, China
[2]Mengcheng National Geophysical Observatory, School of Earth and Space Sciences, University of Science and Technology of China, Hefei, China
[3]Synergetic Innovation Center of Quantum Information and Quantum Physics, University of Science and Technology of China, Hefei, China
[4]Key Laboratory of Earth and Planetary Physics, Institute of Geology and Geophysics, Chinese Academy of Sciences, Beijing, China

Correspondence: Xianghui Xue (xuexh@ustc.edu.cn)

Abstract. On the basis of S4max data retrieved from COSMIC GPS radio occultation measurements, the long-term climatology of the intensity of E_s layers is investigated for the period from December 2006 to January 2014. Global maps of E_s intensity show the high-spatial-resolution geographical distribution and strong seasonal dependence of E_s layers. The maximum intensity of E_s occurs over the midlatitudes, and its value in summer is 2–3 times larger than that in winter. A relatively
5 strong E_s layer is observed at the North and South Poles, with a distinct boundary dividing the midlatitudes and high latitudes along the $60°$–$80°$ geomagnetic latitude band. The simulation results show that the convergence of vertical ion velocity could partially explain the seasonal dependence of E_s intensity. Furthermore, some disagreements between the distributions of the calculated divergence of vertical ion velocity and the observed E_s intensity indicate that other processes, such as the vertical motions of gravity waves, magnetic field effects, meteoric mass influx into Earth's atmosphere and the chemical processes of
10 metallic ions, should also be considered, as they may also play an important role in the spatial and seasonal variations in E_s layers.

1 Introduction

Ionospheric sporadic E (E_s) layers are thin-layered structures with intense, high electron densities at 90–130 km altitudes. Rocket-borne mass spectrometric measurements have shown that the E_s layer mostly result from the ionization of metal atoms,
15 such as Fe^+, Mg^+, and Na^+ (Kopp, 1997; Grebowsky and Aikin, 2002). The E_s layer mainly resides over midlatitudes and is relatively absent at the geomagnetic equator and high latitudes (Whitehead, 1989). It is widely accepted that the mechanism responsible for the E_s layer formation at midlatitudes is the wind shear theory, in which the zonal and meridional winds provide vertical wind shear convergence nodes. As a result, long-lived metallic ions are forced to converge towards the wind shear null to form a thin layer of intense metallic ionization(Whitehead, 1961; Macleod, 1966; Whitehead, 1970; Nygren

et al., 1984; Whitehead, 1989; Haldoupis, 2012). In the equatorial region, the physical process of E_s irregularities is attributed to the gradient-drift instabilities associated with the equatorial electrojet (Tsunoda, 2008). At high magnetic latitudes, the vertical motion of gravity waves is very efficient in concentrating the ionization of E_s because the magnetic field lines are nearly vertical in the polar gap (Bautista et al., 1998; MacDougall et al., 2000a, b; MacDougall and Jayachandran, 2005).

5   The E_s layer generally has a vertical scale of 1 km or less, but its horizontal scale can extend up to several hundreds of kilometres. Consequently, intense E_s plasma irregularities and their sharp vertical electron density gradients seriously affect radio communications and navigation systems (Pavelyev et al., 2007). Furthermore, these effects on global positioning system (GPS) radio occultation (RO) signals detected by low-Earth-orbit (LEO) satellites can be exploited for lower-level atmospheric and ionospheric global investigations (Rocken et al., 2000; Hocke and Tsuda, 2001; Schreiner et al., 2007; Yue et al., 2010,

10   2011).

Observations of E_s layers have been widely investigated from ground-based radars (e.g., Farley, 1985; Whitehead, 1989; Kelly, 1989; Chu and Wang, 1997; Mathews, 1998). In addition to ground-based radars, the scintillations of GPS RO were employed to extensively investigate E_s layers over the past decades (Wu et al., 2005; Arras et al., 2008; Zeng and Sokolovskiy, 2010; Chu et al., 2011). A global map of E_s layers was first presented based on a meridional chain of ionosonde stations

15   (Leighton et al., 1962). In recent years, based on GPS RO measurements, knowledge of the global E_s layer occurrence rate (hereafter called E_sOR) has been remarkably advanced. Wu et al. (2005) used phase and signal-to-noise ratio (SNR) variations from ∼6000 GPS/Challenging Minisatellite Payload (CHAMP) occultations to study the global climatology of E_sOR. Arras et al. (2008) investigated the global E_sOR distribution, with a resolution of $5° \times 5°$, based on CHAMP, GRACE (Gravity Recovery and Climate Experiment), and COSMIC (Constellation Observing System for Meteorology, Ionosphere, and Climate)

20   occultation data. These previous studies of global E_sOR maps show a strong seasonal variation, with a summer maximum in the midlatitudes. Chu et al. (2014) employed COSMIC measurements to study the global morphology of E_sOR and the results of the theoretical simulations suggested that the E_sOR seasonal variation is likely attributed to the convergence of the metallic ion flux caused by vertical wind shear. Shinagawa et al. (2017) calculated the global distribution of the vertical ion convergence and showed that local and seasonal variations in the wind shear distribution could partially account for the geographical and

25   seasonal variation in E_sOR.

Many papers have reported the geographical distribution and seasonal variation in global E_s layers retrieved from GPS RO signals, and nearly all of these works focused on the E_sOR. The global climatology of the intensity of E_s layers has not been fully studied. The purpose of the present paper is to study the global intensity of E_s layers and compare the results of E_s intensity with previous studies on the E_sOR. The occurrence of E_s layers can cause both SNR fluctuations and relative slant

30   total electron content (TEC) peaks (Yue et al., 2015). Sometimes, the SNR has specific U-shape structures in the amplitude of GPS RO signals, as reported by Zeng and Sokolovskiy (2010); Yue et al. (2015). The obvious increase in slant TEC occurring at approximately 92 km implies ionization enhancement in E_s. In this study, the scintillation index (S4 index) data measured from SNR fluctuations in the L1 channel of the COSMIC GPS RO profiles at altitudes between 90 and 130 km for the period from December 2006 to January 2014 are employed to study the global climatology of the ionization of E_s layers. Section 2

35   describes the used data sets and procedures adopted to derive the S4 index. In Section 3, the global long-term behaviours of

E_s layers with a high spatial resolution are presented and compared with the previous E_sOR results, including the latitude-day, latitude-longitude and altitude-latitude distributions; seasonal variations; and geomagnetic dependence of E_s layers. In Section 4, on the basis of the wind shear theory combined with several global-scale models, namely the Whole Atmosphere Community Climate Model (WACCM) (Marsh et al., 2013), the Naval Research Laboratory (NRL) Mass Spectrometer and Incoherent Scatter (MSIS)-00 atmospheric model (Picone et al., 2002), and the International Geomagnetic Reference Field (IGRF)-12 geomagnetic field model (Thébault et al., 2015), we calculate the global distribution of the divergence of metallic ion velocity for comparison with the observations of E_s layers from COSMIC satellites. The effect of the magnetic declination angle on the divergence of the metallic ion velocity in the simulation of E_s is investigated for the first time. Section 5 presents the discussion and conclusions of this paper.

2   Data and Procedure of Deriving the S4 Index

The COSMIC global data sets used in this study are the COSMIC-GPS amplitude S4 indices. The GPS radio signals are received by the precise orbit determination antennas of COSMIC for each GPS RO when a GPS sets or rises behind Earth's atmosphere, as seen by the LEO satellite. Once the GPS signal is received at the LEO satellite, the onboard algorithm of the GPS receiver measures SNR intensity fluctuations from the raw 50 Hz L1 amplitude measurements, which are then recorded in the data stream at a 1 Hz rate at the ground receiver to minimize the data record size (Syndergaard et al., 2006). The raw scintillation measurements from the receiver are therefore the root mean square (RMS) of the SNR intensity fluctuation in one second (i.e., σ_I), which can be expressed as $\sigma_I = \sqrt{\langle (I - \langle I \rangle)^2 \rangle}$. I represents the square of the L1 SNR, and the bracket $\langle \rangle$ denotes the one second averaged value. The S4 indices are reconstructed by the COSMIC Data Analysis and Archive Center (CDAAC) ground processing after these σ_I data are downloaded (Rocken et al., 2000). During the procedure of deriving the S4 indices, two additional steps are included in the ground processing. The first step is to assume that the SNR intensity fluctuations have Gaussian distributions to calculate an approximate value of $\langle I \rangle$ from σ_I and $\langle SNR \rangle$. The second is to apply a low pass filter to the time series of $\langle I \rangle$ to obtain a new average of the intensity $\langle I \rangle_{new}$ at each second to replace the $\langle I \rangle$ in the calculation of the S4 indices. After these steps, a long-term detrended S4 index can be reconstructed by CDAAC ground processing. Further details on the procedure of deriving the S4 index along with some individual example figures can be found in the report of Ko and Yeh (2010).

In the present study, the COSMIC global data sets specifically denote the maximum value of S4 (S4max). The COSMIC global S4max data include the S4max value and geographic latitude, longitude, altitude and local time on which S4max was detected. The computed detrended S4max index is available from 28 December 2006 onwards on the CDAAC website (http://cdaac-www.cosmic.ucar.edu/cdaac). The long-term global climatology of the E_s intensity is investigated based on the global S4max data from December 2006 to January 2014. Figure 1 shows the altitude distribution of the COSMIC S4max profiles. A considerable number of profiles are distributed at altitudes between 40 and 130 km, with a peak number at approximately 100 km. Information on E_s layers can be extracted from amplitude fluctuations in the SNR profiles (Wu et al., 2005). Please note that as a result of the integrated influence either in the SNR or the slant TEC along the LEO-GPS ray, the effect of

E_s layers at high altitudes could map down to the lower tangent point altitudes, which may virtually induce multiple peaks in one RO event (Zeng and Sokolovskiy, 2010; Yue et al., 2015). In Figure 1, the occurrence of sporadic E can be seen down to 40 km as a result of the integral problem of RO measurements. In fact, E_s layers could not be formed by the wind shear theory below 90 km because of the high ion-neutral collision frequencies. The E_s layer over lower altitudes (between 40 and 90 km) should be some artefact resulting from the mapping effect integrated along the LEO-GPS ray. Therefore, the S4max values that appear in altitudes ranging between 90 and 130 km are used to study the E_s layers in the lower ionosphere region. Figure 2 shows the entire distribution of the daily average Es intensity from 2006 to 2014 retrieved from COSMIC within $\pm 2.5°$ latitude and longitude of one ionosonde station in Beijing $(40.3° N, 116.2° E)$, which agrees with the ionosonde measurements $(f_o Es)$. The global morphology of the E_s intensity is presented, and its altitude and seasonal dependences are given at a high spatial resolution because of the large COSMIC RO data sets which have high vertical resolutions.

3   Observations

Figure 3 shows the long-term time series of the E_s values, with a resolution of 5° latitude $\times$ 5 days. As shown, the E_s layer is mainly a sporadic-layered phenomenon in the summer hemisphere, as is known from former E_sOR studies (Leighton et al., 1962; Wu, 2006; Arras et al., 2008; Chu et al., 2014). In Figure 3, it is clear that the intensity of E_s is enhanced in the northern (southern) summer hemisphere from May to September (from November to March), with a maximum in June (December) (i.e., one month ahead of the E_sOR maximum (Chu et al., 2014)). In addition, the seasonal E_s layer also has interannual variability. Compared with the intense Es activity in the summers of 2010 and 2011, the intensity of E_s is lower in the northern summers in 2012 and 2013, respectively. This result may be caused by anomalies in the wind field in the upper atmosphere and a corresponding reduction in the vertical wind shear associated with E_s formation.

The map in Figure 4 shows the global geographical distributions of the E_s average intensity, with a significantly improved spatial resolution of $1° \times 1°$. The red and green solid curves represent the northern and southern geomagnetic latitude contours of 60°, 70°, and 80°, respectively. The geomagnetic equator is also plotted with a yellow curve. The E_s layers are predominantly distributed with S4max values exceeding 0.7 at midlatitudes. Because of the increased spatial resolution, the regional features and longitudinal variations become visible. The intensity of E_s is much weaker at the lower latitudes in both hemispheres, especially in the noticeable gap near the magnetic equator. When the magnetic field is horizontal at the geomagnetic equator, under the zonal wind shear action, ions move vertically by Lorentz forcing. However, they fail to converge into a layer because they are withheld by magnetized electrons. The plasma remains locally neutral. For a meridional wind shear process, ions move along the magnetic field lines with no Lorentz forces acted upon (Haldoupis, 2012). Therefore, a noticeable gap near the magnetic equator could be expected, which is explained by the vanishing vertical component of the geomagnetic field lines, keeping the ionized particles from effectively vertically converging. This gap could also be found in the distribution of E_sOR although it is not as evident in Arras et al. (2008).

Furthermore, the E_s longitudinal variations in the geomagnetic field are also clearly shown. The decrease in E_s intensity can be seen clearly in the Southern Atlantic Anomaly (SAA) zone and the northern American region with geomagnetic latitude.

The region of large E_s intensity exists in the North Africa and North Atlantic regions, Southeast Asian region, South Africa and South Pacific regions. A difference between the E_s intensity and E_sOR distributions is at high latitudes: that is, the occurrence rates of E_s are generally low (Arras et al., 2008), but the intensity of E_s is relatively high. This pattern is more evident over the magnetic poles, which is likely the result of vertical motions of gravity waves in concentrating the ionization of E_s layers (MacDougall et al., 2000a, b). The lower panels depict the northern and southern polar views of the distributions of E_s intensity, and these views make the features clearer.

The maps in Figure 5 show the geographical distribution of E_s intensity for four different seasons in a $1° \times 1°$ grid. The distribution of E_s layers shows a significant seasonal dependence. The intensity of the E_s layers in the midlatitudes of the summer hemisphere is 2–3 times larger than that in the winter hemisphere. During equinox seasons, the intensity of the E_s layers moderately covers the entire globe, and a distinct boundary dividing the midlatitudes and high latitudes is visible along the $60°–80°$ geomagnetic latitude band. From the polar views during each season, it can be seen that the E_s layers remain at a relatively high level in the North and South Poles. This characteristic could be attributed to high energy radiation, particle precipitation and polar gap gravity waves.

Figure 6 shows the altitude-latitude distribution of the E_s intensity with a resolution of 1 km altitude $\times$ 1° latitude. The intensity of E_s is distributed at altitudes between 95 and 125 km. The densest patches of E_s exist at altitudes exceeding 110 km, which is different from the E_sOR altitude-latitude distribution that dominates at 95–110 km, with a peak at approximately 105 km in the midlatitudes of $25°–45°$(Arras et al., 2008). The E_s intensity has a broader latitudinal extent of $10°S–75°S$ in the Southern Hemisphere, compared with $10°N–60°N$ in the Northern Hemisphere.

Figure 7 presents the seasonal variation in the altitude-latitude distributions of the E_s intensity for the same temporal period and spatial resolution as those in Figure 6. The E_s intensity for the summer and winter solstices clearly has a significantly broader latitudinal extent towards the high latitude region. In addition, the overall intensities of the E_s layers increase, spanning a larger vertical extent during the solstices. In general, the E_s intensity exceeding 0.65 values is distributed at altitudes of 100– 125 km in the southern summer and at altitudes of 90–130 km in the northern summer. During equinox seasons, the E_s intensity is moderate and its altitude-latitude distribution is relatively symmetric.

4 Wind Shear Theory Explanation for E_s Seasonal Variation

The global climatology of the intensity of E_s layers is investigated from the COSMIC occultation data employing the GPS RO technique. One of the pronounced variabilities in E_s layers is the seasonal variation, with a maximum appearance in the summer hemisphere. Although the mechanism for E_s layer formation is widely accepted, these dense and thin layers of metallic ion plasma are formed by the vertical ion convergence of neutral wind shear. The overall morphology of E_s layers cannot be explained by the wind shear theory. One of the unsolved issues in the ionosphere is that the overall morphology, including the seasonal dependence of Es layers, does not have a comprehensive explanation (Whitehead, 1989; Haldoupis et al., 2007).

Seasonal dependence is found not only in the E_s intensity but also in previous studies of E_sOR variations (Wu et al., 2005; Arras et al., 2008; Chu et al., 2014). Chu et al. (2014) simulated the global distribution of the convergence of metallic ion flux

caused by vertical wind shear, suggesting that the maximum E_s in summer and minimum of E_s in winter are likely caused by the vertical wind shear effect.

From the wind shear theory (e.g., Nygren et al., 1984; Mathews, 1998; Kirkwood and Nilsson, 2000), the vertical ion velocity w_i induced by the neutral wind is described by equation (1):

$$5 \quad w_i = \frac{r_i cos I}{1 + r_i^2} \times U - \frac{sin I cos I}{1 + r_i^2} \times V + \frac{r_i^2 + sin^2 I}{1 + r_i^2} \times W \qquad (1)$$

where I represents the magnetic inclination angle that is defined as positive (i.e., downward direction) in the Northern Hemisphere, r_i represents the ratio of the ion-neutral collision frequency (ν_i) to the ion gyrofrequency (ω_i), and the neutral wind velocity $V_n = (U, V, W)$ components are in the zonal (positive for eastward), meridional (positive for northward), and vertical (positive for upward) directions. Therefore, the favourable wind field for E_s layer formation is where there is a negative
10    $\frac{dw_i}{dz}$ relationship, indicating an ion-convergence region.

Version 4 of the WACCM (WACCM4) is a global climate model with interactive chemistry, developed at the National Center for Atmospheric Research (NCAR) (Marsh et al., 2013). A specified dynamics run of WACCM4 (SD-WACCM4) was constrained by the Modern-Era Retrospective Analysis for Research and Applications (MERRA). SD-WACCM4 is used to simulate the global distribution of the divergence of ion velocity from the period of 2006 to 2014, which is consistent with the
15   period of E_s observations from the COSMIC occultation data. To compare with previous studies, the neutral wind is provided by the output from WACCM, and the ion-neutral frequency is calculated by the atmospheric composition from the MSIS-00 atmospheric model in accordance with Chu et al. (2014). The global distributions of the geomagnetic field and magnetic inclination angle at 100 km are estimated from the IGRF-12 model. The calculation of ion velocity is binned and averaged in a $1°$ latitude $\times$ $1°$ longitude grid at WACCM altitude levels from 0–130 km.
20   Figure 8 presents simulation results of the global distributions of the monthly mean divergence in vertical ion velocity in the altitude range between 97 and 114 km in January and July. The negative (positive) $\frac{dw_i}{dz}$ ratio represents the convergence (divergence) of ions in units of $ms^{-1}km^{-1}$. Ihe results show a good correlation between the simulated distributions of the monthly mean divergence of vertical ion velocity in Figure 8 and the geographical distribution of E_s intensity measured from the COSMIC GPS RO profiles in Figure 5. Chu et al. (2014) simulated the global distributions of the mean divergence of
25   the Fe^+ concentration flux at altitudes of 94–115 km in all four seasons. The study also showed a similar simulation result of the distributions of divergence in the Fe^+ concentration flux, which is well correlated with the COSMIC-measured E_sOR distribution. The simulation of the divergence of vertical ion velocity supports the wind shear theory for E_s formation and indicates that the seasonal dependence of E_s layers is likely attributed to the convergence of vertical ion velocity driven by neutral wind.
30   Furthermore, we also notice that the E_s intensity is distributed at relatively higher altitudes of 95–125 km compared with the E_sOR at 90–120 km. The densest patches of E_s exist above 115 km, and the E_s layer has a broader vertical extent in summer, as shown in Figure 7. In the simulation, the distributions of the monthly mean divergence of the vertical ion velocity at an altitude range of 114–128 km in January and July are shown in Figure 9. In contrast to the distributions of the divergence of

vertical ion velocity between 97 and 114 km in Figure 8, Figure 9 shows an ion-divergence region at altitudes of 114–128 km in summer over midlatitudes as a result of different zonal and meridional winds. These results suggest that the wind shear theory alone has difficulty explaining the E_s seasonal dependence at higher altitudes (114–128 km), although the wind shear theory is considered the primary theory to explain the physical production of E_s layers (Whitehead, 1989; Haldoupis et al., 2007).

5   In previous studies on the wind shear theory for E_s layer formation, the magnetic declination angle effect is neglected in the calculation of the vertical ion velocity w_i induced by the neutral wind. The steady-state ion momentum equation is:

$$m\frac{\mathrm{d}\boldsymbol{v}_i}{\mathrm{d}t} = 0 = e(\boldsymbol{E} + \boldsymbol{v}_i \times \boldsymbol{B}) - M\nu_{in}(\boldsymbol{v}_i - \boldsymbol{V}_n) \tag{2}$$

On the basis of the steady-state ion momentum equation, the equation (1) for the vertical ion velocity w_i is extended to take the magnetic declination angle D into consideration as follows:

10    $$w_i = \frac{r_i cosDcosI - sinDsinIcosI}{1 + r_i^2} \times U - \frac{r_i sinDcosI + cosDsinIcosI}{1 + r_i^2} \times V + \frac{r_i^2 + sin^2I}{1 + r_i^2} \times W \tag{3}$$

The magnetic declination angle currently ranges from -30° (west) to 26° (east); therefore its influence on the vertical ion velocity w$_i$ is expected. The effect of the magnetic declination angle on the divergence in ion velocity in the simulation of E_s is investigated. Figure 10 presents the global distributions of the monthly mean divergence in vertical ion velocity at altitudes ranging from 97–114 km with the consideration of the magnetic declination angle. The figure shows a seasonal dependence,

15   with ion-convergence regions in summer and ion-divergence regions in winter. However, the morphology of the divergence of the vertical ion velocity is different from that without the magnetic declination angle considere in Figure 8. In January, strong ion convergence appears in the SAA region. In July, Asia, Europe, and the North Pacific tend to be regions of ion convergence. The agreement with the observations becomes worse, which could imply that the cause of global E_s layers remains a mystery because it cannot be fully accounted for by the wind shear effect (Whitehead, 1989; Haldoupis et al., 2007). The formation

20   of mid-latitude E_s layers could be partially explained by the wind shear theory. The investigation of the causes of seasonal variability in E_s should lead to more detailed studies to fully understand and properly quantify the properties of E_s layers.

5   Discussion

The seasonal and geographical dependences of E_sOR have been widely studied by ionospheric observations since 1960s (Leighton et al., 1962; Smith, 1978; Wu et al., 2005; Arras et al., 2008; Zeng and Sokolovskiy, 2010), but, thus far, the overall

25   morphology of E_s is still not well explained. The seasonal dependence of E_s layers remains an ongoing mystery, as it is unexpected in the classical wind shear theory reported in the review article of Whitehead (1989). Recently, Chu et al. (2014) simulated the distribution of the convergence of the Fe$^+$ concentration flux and indicated that the vertical ion convergence caused by neutral wind could be responsible for the seasonal dependence of E_s.

In our investigations, the global climatology of the intensity of E_s layers is found to also have a seasonal dependence, with a

30   pronounced maximum over midlatitudes in the summer hemisphere, as shown in Figure 5. The E_s intensity has similar seasonal

and spatial distributions as the E_sOR, but the E_s layer has a relatively large intensity and a small E_sOR value at the North and South Poles. The wind shear mechanism does not work efficiently at either auroral zones or the magnetic equator (Haldoupis, 2012); therefore, the strong E_s layers in the Earth's polar regions could be initially caused by gravity waves (Bautista et al., 1998; MacDougall et al., 2000a, b). In the simulations, the gravity waves with horizontal wavelengths smaller than ~200 km are not explicitly resolved in WACCM (Liu et al., 2014). In particular, the vertical motion of gravity waves dominates the formation of the E_s layer in the polar cap, where the near-vertical magnetic field significantly reduces the effectives of wind-shear in converging ions into layers. Polar cap gravity waves have been studied by Johnson et al. (1995); MacDougall et al. (1997). These layers are maintained in an ionized state by charge exchange of neutral metal atoms with NO^+ and $O_2{}^+$ ions by photoionization. These studies found that the vertical motion of gravity waves is very efficient in concentrating polar cap E_s layers. The short-lived polar cap E_s layers in winter appear to be associated with gravity waves. The polar cap E_s layers in summer are long-lasting thin layers. These initial concentrations of metallic ions persist and change into long-lived E_s because of ambient metallic ions. The E_s layers at the cusp latitude are relatively different from those at the polar cap. The cusp E_s could be associated with the convergence of ionization by the electric fields (MacDougall and Jayachandran, 2005).

On the other hand, simulating the global distributions of the monthly mean divergence of vertical ion velocity in an altitude range between 97 and 114 km shows an ion-convergence region in the summer midlatitudes, which is similar to the simulation results of Chu et al. (2014). This result suggests that the seasonal dependence of E_s is likely attributed to the vertical convergence of ions driven by neutral wind. However, some disagreements between the distributions of the calculated divergence of vertical ion velocity and observed E_s intensity are found. For example, there are ion-divergence regions in the midlatitudes in winter in Figure 8, but the dissipation of E_s is observed in the 60°–80° geomagnetic latitude band. The densest E_s layer appears above 115 km, which is higher than the E_sOR. Another discrepancy is that the simulated divergence of vertical ion velocity in an altitude range between 114 and 128 km has a positive $\frac{\mathrm{d}w_i}{\mathrm{d}z}$ ratio in the summer hemisphere, which indicates an ion-divergence region of ions in contrast to the observed summer maximum of E_s intensity in the summer midlatitudes.

The effect of the magnetic declination angle on the divergence of metallic ion velocity is investigated in the simulation of E_s for the first time in Figure 10. Though the figure shows marked seasonal dependence, with a strong summer ion-convergence region, the morphology of the divergence of vertical ion velocity is different from the distribution of the observed E_s intensity in Figure 5. Thus, the vertical ion convergence by itself is far from sufficient for explaining the strong E_s summer maximum. Other physical processes should also be considered in the geographical distribution and spatial variations in E_s layers, as they play important roles in determining the global morphology of E_s such as the magnetic field, ionospheric electric field, the chemical processes of metallic ions, large geomagnetic storms, and meteorological processes in the lower atmosphere (e.g., Bautista et al., 1998; Mathews, 1998; Carter and Forbes, 1999; MacDougall et al., 2000a, b; Davis and Johnson, 2005; MacDougall and Jayachandran, 2005; Johnson and Davis, 2006; Haldoupis, 2012; Yue et al., 2012; Feng et al., 2013; Yu et al., 2015).

Haldoupis et al. (2007) proposed that the seasonal dependence of E_s could be explained by the seasonal variation in the meteor influx into the upper atmosphere. However, it has been largely accepted that sporadic meteoroids provide a much greater meteor mass on average than meteor showers (Ceplecha et al., 1998; Baggaley, 2002; Janches et al., 2002; Williams

and Murad, 2002). The meteoric mass influx caused by sporadic meteoroids reaches a maximum in autumn rather than summer (Janches et al., 2006). The global input of meteoric material is well established to enhance the mesospheric metal layers and E_s layers (Plane, 2004; Carrillo-Sánchez et al., 2015; Plane et al., 2015), but the daily amount is still not well defined, and estimates of the global interplanetary dust particles (IDPs) range from 5–270 tonnes per day (Plane, 2012; Carrillo-Sánchez et al., 2016). These effects of meteoric ablation are significantly influenced by the magnitude of the IDP input by two orders of magnitude uncertainty. On the other hand, this fact also highlights the importance of fundamental understanding of the global climatology of E_s layers.

6 Conclusions

In this study, we investigate the long-term climatology of the intensity of E_s layers on the basis of S4max data retrieved from COSMIC GPS RO measurements. The resulting global E_s maps with a high spatial resolution present the geographical distributions and strong seasonal dependence of E_s intensity, which agrees with former studies of global E_sOR maps (Wu, 2006; Arras et al., 2008; Chu et al., 2014). The high E_s intensity in summer exists at altitudes of 115–125 km at 10°–60° latitude in the Northern Hemisphere, and at altitudes of 115–120 km in the 10°–75° latitudes in the Southern Hemisphere.

Furthermore, the simulation results of the global distributions of the monthly mean divergence of vertical ion velocity could partially explain the seasonal dependence of E_s intensity. We show that the elemental mechanism responsible for E_s layers based on the wind shear theory could explain the seasonal dependence of Es intensity (97–114 km), but it is hard to explain the Es seasonal dependence at higher altitudes (114–128 km). To further investigate the magnetic field effects on the wind shear processes of E_s formation, the effect of the magnetic declination angle on the divergence of metallic ion velocity in the simulation of E_s is investigated, and we discuss some disagreements between the distributions of the calculated divergence of vertical ion velocity and the observed E_s intensity. Although the wind shear theory for the E_s formation was conceived and formulated in 1960s (Whitehead, 1961), its importance for understanding the formation of E_s must have escaped attention. This study implies that, in addition to the vertical wind shear effects, other processes, such as the vertical motion of gravity waves, magnetic field effects, meteoric mass influx into Earth's atmosphere and the chemical processes of metallic ions, should also be considered, which could play a dominant role in the geographical and seasonal variations in E_s layers. To accurately understand and properly quantify the properties of E_s layers at a global scale that are also associated with the distribution of global metallic ions, we need to combine more ground-based ionosonde data with satellite observations and extensively study the geographical and seasonal variations in E_s layers.

5

References

Arras, C., Wickert, J., Beyerle, G., Heise, S., Schmidt, T., and Jacobi, C.: A global climatology of ionospheric irregularities derived from GPS radio occultation, Geophysical research letters, 35, 2008.

Baggaley, W. J.: Radar observations, Cambridge University Press, Cambridge, 2002.

5 Bautista, M. A., Romano, P., and Pradhan, A. K.: Resonance-averaged photoionization cross sections for astrophysical models, The Astrophysical Journal Supplement Series, 118, 259–265, 1998.

Carrillo-Sánchez, J. D., Plane, J. M. C., Feng, W., Nesvornỳ, D., and Janches, D.: On the size and velocity distribution of cosmic dust particles entering the atmosphere, Geophysical research letters, 42, 6518–6525, 2015.

Carrillo-Sánchez, J. D., Nesvornỳ, D., Pokornỳ, P., Janches, D., and Plane, J. M. C.: Sources of cosmic dust in the Earth's atmosphere, 10 Geophysical research letters, 43, 2016.

Carter, L. N. and Forbes, J. M.: Global transport and localized layering of metallic ions in the upper atmosphere, 17, 190–209, 1999.

Ceplecha, Z., Borovička, J., Elford, W. G., ReVelle, D. O., Hawkes, R. L., Porubčan, V., and Šimek, M.: Meteor phenomena and bodies, Space Science Reviews, 84, 327–471, 1998.

Chu, Y., Wang, C., Wu, K., Chen, K., Tzeng, K. J., Su, C., Feng, W., and Plane, J. M. C.: Morphology of sporadic E layer retrieved from 15 COSMIC GPS radio occultation measurements: Wind shear theory examination, Journal of Geophysical Research: Space Physics, 119, 2117–2136, 2014.

Chu, Y.-H. and Wang, C.-Y.: Interferometry observations of three-dimensional spatial structures of sporadic E irregularities using the Chung-Li VHF radar, Radio Science, 32, 817–832, 1997.

Chu, Y.-H., Brahmanandam, P. S., Wang, C.-Y., Su, C.-L., and Kuong, R.-M.: Coordinated sporadic E layer observations made with Chung-20 Li 30 MHz radar, ionosonde and FORMOSAT-3/COSMIC satellites, Journal of Atmospheric and Solar-Terrestrial Physics, 73, 883–894, 2011.

Davis, C. J. and Johnson, C. G.: Lightning-induced intensification of the ionospheric sporadic E layer, Nature, 435, 799, 2005.

Farley, D. T.: Theory of equatorial electrojet plasma waves-new developments and current status, Journal of Atmospheric and Terrestrial Physics, 47, 729–744, 1985.

25 Feng, W., Marsh, D. R., Chipperfield, M. P., Janches, D., Höffner, J., Yi, F., and Plane, J. M. C.: A global atmospheric model of meteoric iron, Journal of Geophysical Research: Atmospheres, 118, 9456–9474, 2013.

Grebowsky, J. M. and Aikin, A. C.: In Situ Measurements of Meteoric Ions, 2002.

Haldoupis, C.: Midlatitude sporadic E. A typical paradigm of atmosphere-ionosphere coupling, Space science reviews, 168, 441–461, 2012.

Haldoupis, C., Pancheva, D., Singer, W., Meek, C., and MacDougall, J.: An explanation for the seasonal dependence of midlatitude sporadic 30 E layers, Journal of Geophysical Research: Space Physics, 112, 2007.

Hocke, K. and Tsuda, T.: Gravity waves and ionospheric irregularities over tropical convection zones observed by GPS/MET radio occultation, Geophysical Research Letters, 28, 2815–2818, 2001.

Janches, D., Pellinen-Wannberg, A., Wannberg, G., Westman, A., Häggström, I., and Meisel, D. D.: Tristatic observations of meteors using the 930 MHz European Incoherent Scatter radar system, Journal of Geophysical Research: Space Physics, 107, 2002.

35 Janches, D., Heinselman, C. J., Chau, J. L., Chandran, A., and Woodman, R.: Modeling the global micrometeor input function in the upper atmosphere observed by high power and large aperture radars, Journal of Geophysical Research: Space Physics, 111, 2006.

Johnson, C. G. and Davis, C. J.: The location of lightning affecting the ionospheric sporadic-E layer as evidence for multiple enhancement mechanisms, Geophysical research letters, 33, 2006.

Johnson, F. S., Hanson, W. B., Hodges, R. R., Coley, W. R., Carignan, G. R., and Spencer, N. W.: Gravity waves near 300 km over the polar caps, Journal of Geophysical Research: Space Physics, 100, 23 993–24 002, 1995.

5   Kelly, M. C.: The Earth's ionosphere, Int. Geophys. Ser, 43, 71, 1989.

Kirkwood, S. and Nilsson, H.: High-latitude sporadic-E and other thin layers–the role of magnetospheric electric fields, Space Science Reviews, 91, 579–613, 2000.

Ko, C. P. and Yeh, H. C.: COSMIC/FORMOSAT-3 observations of equatorial F region irregularities in the SAA longitude sector, Journal of Geophysical Research: Space Physics, 115, 2010.

10   Kopp, E.: On the abundance of metal ions in the lower ionosphere, Journal of Geophysical Research: Space Physics, 102, 9667–9674, 1997.

Leighton, H. I., Shapley, A. H., and Smith, E. K.: The occurrence of sporadic E during the IGY, in: Ionospheric Sporadic, pp. 166–177, Elsevier, 1962.

Liu, H.-L., McInerney, J. M., Santos, S., Lauritzen, P. H., Taylor, M. A., and Pedatella, N. M.: Gravity waves simulated by high-resolution whole atmosphere community climate model, Geophysical Research Letters, 41, 9106–9112, 2014.

15   MacDougall, J. W. and Jayachandran, P. T.: Sporadic E at cusp latitudes, Journal of atmospheric and solar-terrestrial physics, 67, 1419–1426, 2005.

MacDougall, J. W., Hall, G. E., and Hayashi, K.: F region gravity waves in the central polar cap, Journal of Geophysical Research: Space Physics, 102, 14 513–14 530, 1997.

MacDougall, J. W., Jayachandran, P. T., and Plane, J. M. C.: Polar cap Sporadic-E: part 1, observations, Journal of Atmospheric and Solar-
20   Terrestrial Physics, 62, 1155–1167, 2000a.

MacDougall, J. W., Plane, J. M. C., and Jayachandran, P. T.: Polar cap Sporadic-E: part 2, modeling, Journal of Atmospheric and Solar-Terrestrial Physics, 62, 1169–1176, 2000b.

Macleod, M. A.: Sporadic E theory. I. Collision-geomagnetic equilibrium, Journal of the Atmospheric Sciences, 23, 96–109, 1966.

Marsh, D. R., Mills, M. J., Kinnison, D. E., Lamarque, J.-F., Calvo, N., and Polvani, L. M.: Climate change from 1850 to 2005 simulated in
25   CESM1 (WACCM), Journal of climate, 26, 7372–7391, 2013.

Mathews, J. D.: Sporadic E: current views and recent progress, Journal of atmospheric and solar-terrestrial physics, 60, 413–435, 1998.

Nygren, T., Jalonen, L., Oksman, J., and Turunen, T.: The role of electric field and neutral wind direction in the formation of sporadic E-layers, Journal of Atmospheric and Terrestrial Physics, 46, 373–381, 1984.

Pavelyev, A. G., Liou, Y. A., Wickert, J., Schmidt, T., Pavelyev, A. A., and Liu, S.-F.: Effects of the ionosphere and solar activity on radio
30   occultation signals: Application to CHAllenging Minisatellite Payload satellite observations, Journal of Geophysical Research: Space Physics, 112, 2007.

Picone, J. M., Hedin, A. E., Drob, D. P., and Aikin, A. C.: NRLMSISE-00 empirical model of the atmosphere: Statistical comparisons and scientific issues, Journal of Geophysical Research: Space Physics, 107, 2002.

Plane, J. M. C.: A time-resolved model of the mesospheric Na layer: constraints on the meteor input function, Atmospheric Chemistry and
35   Physics, 4, 627–638, 2004.

Plane, J. M. C.: Cosmic dust in the Earth's atmosphere, Chemical Society Reviews, 41, 6507–6518, 2012.

Plane, J. M. C., Feng, W., and Dawkins, E. C. M. D.: The mesosphere and metals: Chemistry and changes, Chemical reviews, 115, 4497–4541, 2015.

12

Rocken, C., Ying-Hwa, K., Schreiner, W. S., Hunt, D., Sokolovskiy, S., and McCormick, C.: COSMIC system description, Terrestrial Atmospheric and Oceanic Sciences, 11, 21–52, 2000.

Schreiner, W., Rocken, C., Sokolovskiy, S., Syndergaard, S., and Hunt, D.: Estimates of the precision of GPS radio occultations from the COSMIC/FORMOSAT-3 mission, Geophysical Research Letters, 34, 2007.

5 Shinagawa, H., Miyoshi, Y., Jin, H., and Fujiwara, H.: Global distribution of neutral wind shear associated with sporadic E layers derived from GAIA, Journal of Geophysical Research: Space Physics, 122, 4450–4465, 2017.

Smith, E. K.: Temperate zone sporadic-E maps (f0Es > 7 MHz), Radio Science, 13, 571–575, 1978.

Syndergaard, S., Schreiner, W. S., Rocken, C., Hunt, D. C., and Dymond, K. F.: Preparing for COSMIC: Inversion and analysis of ionospheric data products, in: Atmosphere and Climate, pp. 137–146, Springer, 2006.

10 Thébault, E., Finlay, C. C., Beggan, C. D., Alken, P., Aubert, J., Barrois, O., Bertrand, F., Bondar, T., Boness, A., Brocco, L., et al.: International geomagnetic reference field: the 12th generation, Earth, Planets and Space, 67, 79, 2015.

Tsunoda, R. T.: On blanketing sporadic E and polarization effects near the equatorial electrojet, Journal of Geophysical Research: Space Physics, 113, 2008.

Whitehead, J. D.: The formation of the sporadic-E layer in the temperate zones, Journal of Atmospheric and Terrestrial Physics, 20, 49–58,
15   1961.

Whitehead, J. D.: Production and prediction of sporadic E, Reviews of Geophysics, 8, 65–144, 1970.

Whitehead, J. D.: Recent work on mid-latitude and equatorial sporadic-E, Journal of Atmospheric and Terrestrial Physics, 51, 401–424, 1989.

Williams, I. P. and Murad, E.: Meteors in the Earth's Atmosphere, Cambridge University Press, Cambridge, 2002.

20 Wu, D. L.: Small-scale fluctuations and scintillations in high-resolution GPS/CHAMP SNR and phase data, Journal of atmospheric and solar-terrestrial physics, 68, 999–1017, 2006.

Wu, D. L., Ao, C. O., Hajj, G. A., de La Torre Juarez, M., and Mannucci, A. J.: Sporadic E morphology from GPS-CHAMP radio occultation, Journal of Geophysical Research: Space Physics, 110, 2005.

Yu, B., Xue, X., Lu, G., Ma, M., Dou, X., Qie, X., Ning, B., Hu, L., Wu, J., and Chi, Y.: Evidence for lightning-associated enhancement of
25   the ionospheric sporadic E layer dependent on lightning stroke energy, Journal of Geophysical Research: Space Physics, 120, 9202–9212, 2015.

Yue, J., Wang, W., Richmond, A. D., and Liu, H.-L.: Quasi-two-day wave coupling of the mesosphere and lower thermosphere-ionosphere in the TIME-GCM: Two-day oscillations in the ionosphere, Journal of Geophysical Research: Space Physics, 117, 2012.

Yue, X., Schreiner, W. S., Lei, J., Rocken, C., Hunt, D. C., Kuo, Y.-H., and Wan, W.: Global ionospheric response observed by COSMIC
30   satellites during the January 2009 stratospheric sudden warming event, Journal of Geophysical Research: Space Physics, 115, 2010.

Yue, X., Schreiner, W. S., Hunt, D. C., Rocken, C., and Kuo, Y.-H.: Quantitative evaluation of the low Earth orbit satellite based slant total electron content determination, Space Weather, 9, 2011.

Yue, X., Schreiner, W. S., Zeng, Z., Kuo, Y., and Xue, X.: Case study on complex sporadic E layers observed by GPS radio occultations, Atmospheric Measurement Techniques, 8, 225, 2015.

35 Zeng, Z. and Sokolovskiy, S.: Effect of sporadic E clouds on GPS radio occultation signals, Geophysical Research Letters, 37, 2010.
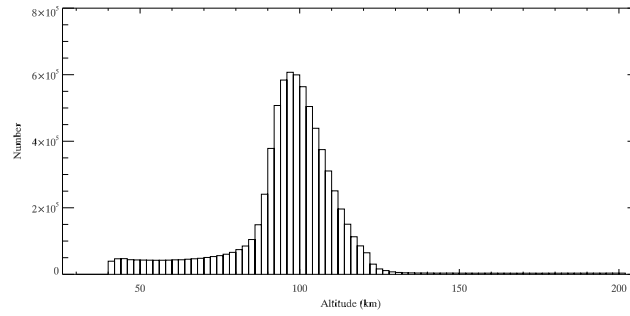
Figure 1. The altitude distribution of COSMIC S4max profiles from December 2006 to January 2014.
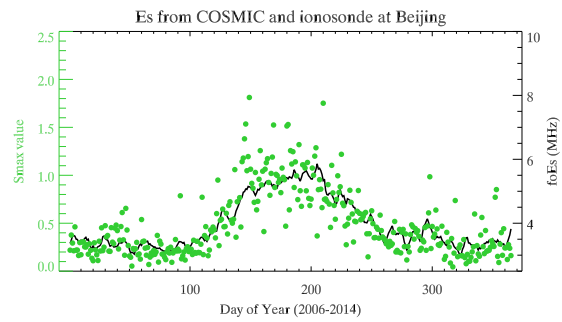
Figure 2. The entire distribution of the daily average Es intensity retrieved from COSMIC within $\pm\ 2.5°$ latitude and longitude of one ionosonde station and ionosonde data ($f_o Es$) in Beijing from 2006 to 2014.
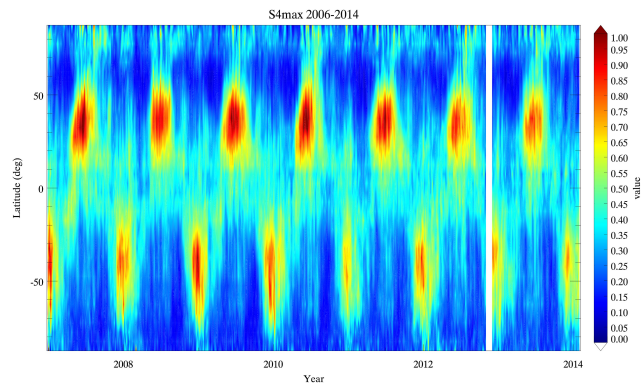
Figure 3. Time series of the E_s intensity with a resolution of 5° latitude × 5 days for the period from December 2006 to January 2014.
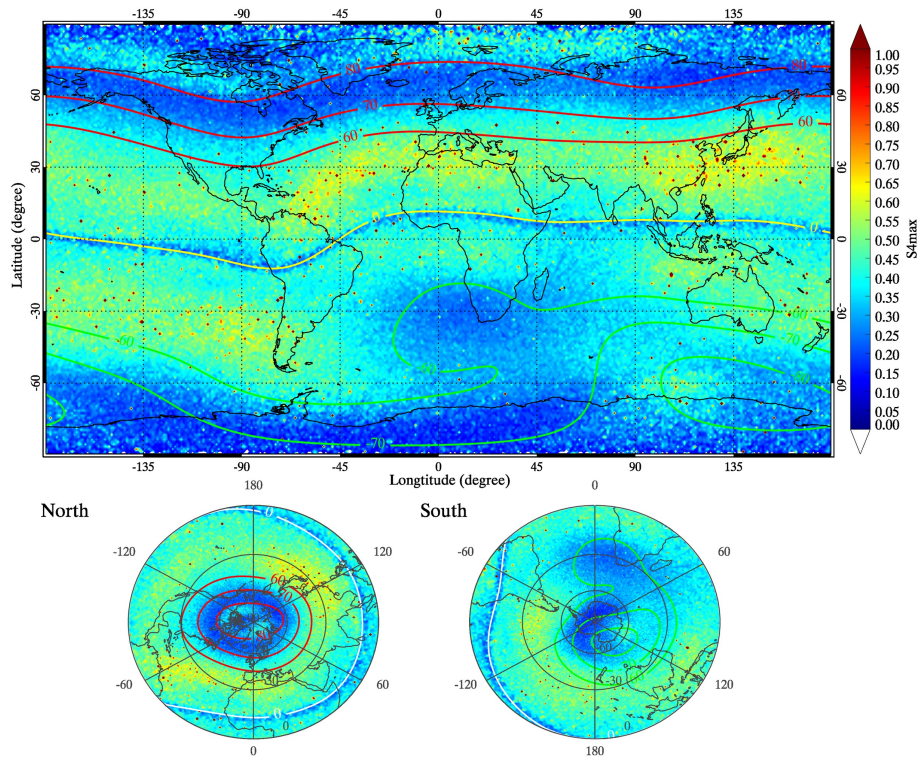
Figure 4. Global geographical distributions of the E_s average intensity from 2006 to 2014, with a spatial resolution of a $1° \times 1°$ grid. The red and green curves signify the geomagnetic latitude contours of $60°$, $70°$, and $80°$, and the yellow curve represents the geomagnetic equator.

Figure 5. Seasonal variations in E_s intensity from 2006 to 2014, with a spatial resolution of a $1° \times 1°$ grid. Plots for (a) autumn (September, October, November), (b) winter (December, January, February), (c) spring (March, April, May), and (d) summer (June, July, August).
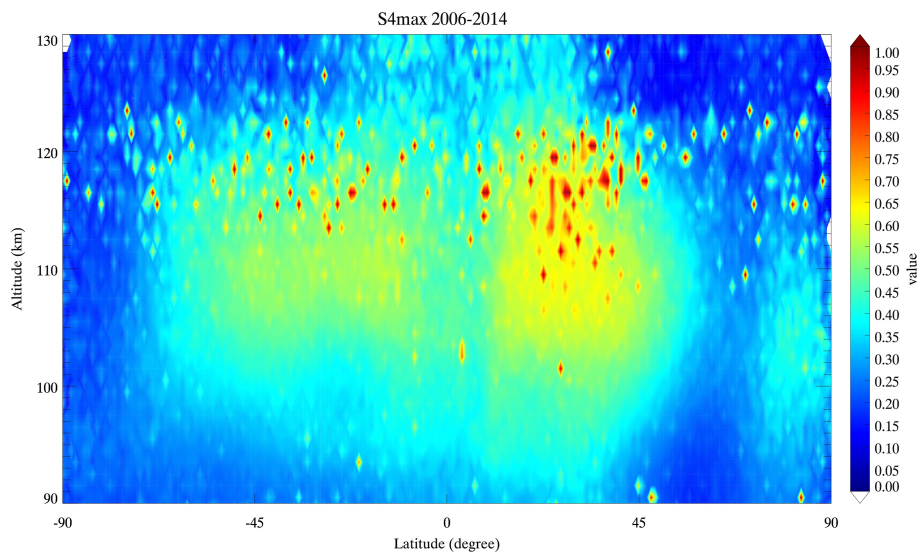
Figure 6. Altitude-latitude distribution of the E_s intensity from 2006 to 2014, with a resolution of 1 km altitude $\times$ 1° latitude.
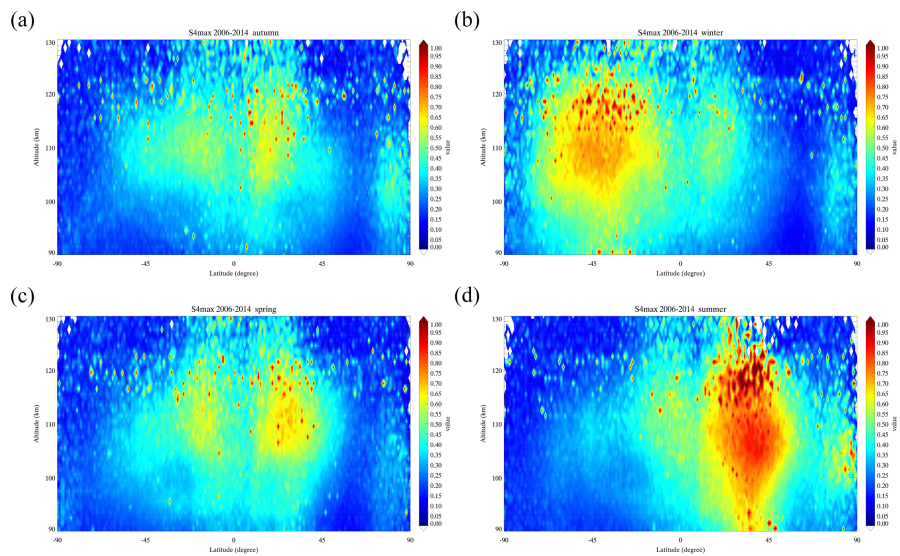
Figure 7. Seasonal variations in altitude-latitude distributions of E_s intensity from 2006 to 2014 for four different seasons: (a) autumn, (b) winter, (c) spring, and (d) summer.
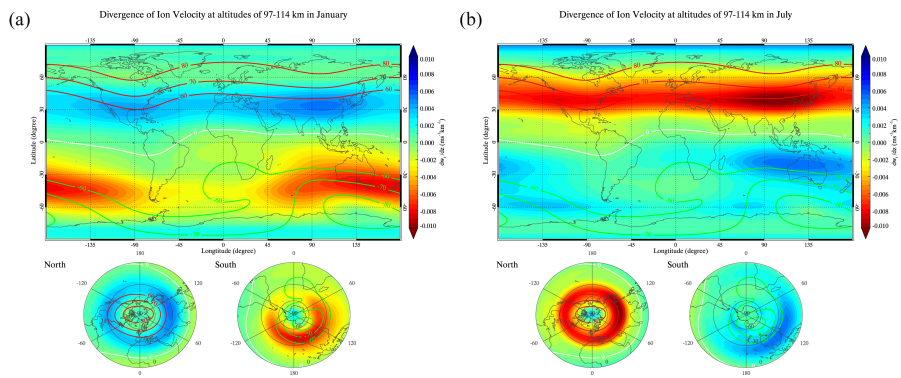
Figure 8. Simulation results of the global distributions of the monthly mean divergence of vertical ion velocity from 2006 to 2014 (units of $ms^{-1}km^{-1}$) at altitudes ranging between 97 and 114 km in January (a) and July (b). The red and green curves signify $60°$, $70°$, and $80°$ geomagnetic latitude contours, and the yellow curve represents the geomagnetic equator.
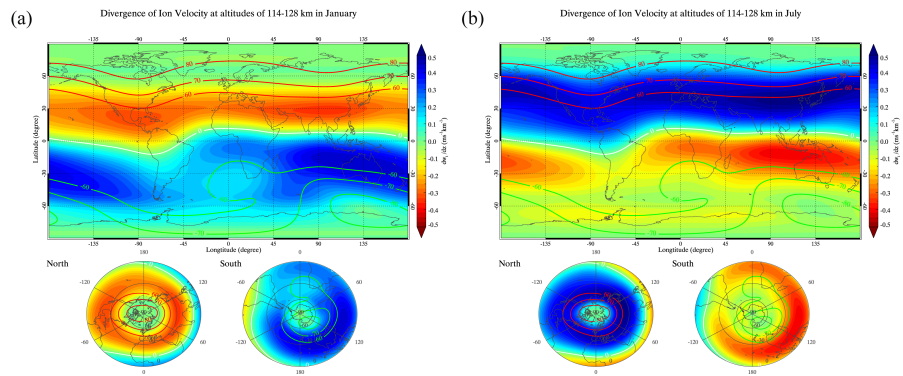
Figure 9. Same as Figure 8 but for the altitude range between 114 and 128 km in January (a) and July (b).

(a) Divergence of Ion Velocity at altitudes of 97-114 km in January

(b) Divergence of Ion Velocity at altitudes of 97-114 km in July

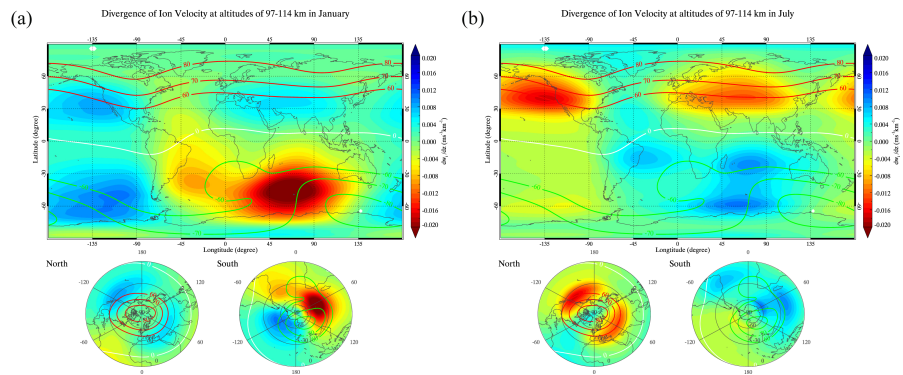North   South   North   South

Figure 10. Same as Figure 8 but with the consideration of the effect of the magnetic declination angle on the vertical ion velocity in January (a) and July (b).